

**Electronic band structure and proximity to magnetic ordering in the  
chiral cubic compound CrGe**

Klotz, J.; Götze, K.; Förster, T.; Bruin, J. A. N.; Wosnitzer, J.; Weber, K.; Schmidt, M.;  
Schnelle, W.; Geibel, C.; Rößler, U. K.; Rosner, H.;

Originally published:

February 2019

**Physical Review B 99(2019), 085130**

DOI: <https://doi.org/10.1103/PhysRevB.99.085130>

Perma-Link to Publication Repository of HZDR:

<https://www.hzdr.de/publications/Publ-28921>

Release of the secondary publication  
on the basis of the German Copyright Law § 38 Section 4.

# Electronic band structure and proximity of magnetic ordering in the chiral cubic compound CrGe

J. Klotz,<sup>1,2,\*</sup> K. Götze,<sup>1,2,†</sup> T. Förster,<sup>1</sup> J. A. N. Bruin,<sup>3</sup> J. Wosnitza,<sup>1,2</sup> K. Weber,<sup>4</sup> M. Schmidt,<sup>4</sup> W. Schnelle,<sup>4</sup> C. Geibel,<sup>4</sup> U. K. Rößler,<sup>5</sup> and H. Rosner<sup>4,‡</sup>

<sup>1</sup>*Hochfeld-Magnetlabor Dresden (HLD-EMFL), Helmholtz-Zentrum Dresden-Rossendorf, 01328 Dresden, Germany*

<sup>2</sup>*Institut für Festkörper- und Materialphysik, Technische Universität Dresden, 01062 Dresden, Germany*

<sup>3</sup>*High Field Magnet Laboratory (HFML-EMFL), Radboud University, 6525 ED, Nijmegen, The Netherlands*

<sup>4</sup>*Max Planck Institute for Chemical Physics of Solids, 01187 Dresden, Germany*

<sup>5</sup>*Leibniz Institute for Solid State and Material Research IFW, 01069 Dresden, Germany*

(Dated: December 19, 2018)

CrGe belongs to the family of cubic B20 intermetallics. From experimental investigations by susceptibility and de Haas-van Alphen (dHvA) measurements and from calculations of its electronic band-structure by density-functional theory (DFT), CrGe is found to form a metallic paramagnetic ground state. Combining dHvA and DFT data, a detailed picture of the Fermi surface of CrGe is provided. The proximity to a magnetic long-range ordering in CrGe is suggested from a prominent thermal magnetic susceptibility. The possibility to induce magnetic long-range order in CrGe is discussed based on calculated properties for CrGe substituting Ge by As or Sn, and from a comparison with MnGe and the alloy series  $\text{Cr}_{1-x}\text{Mn}_x\text{Ge}$ . Owing to the noncentrosymmetric and nonsymmorphic crystal structure of CrGe, in absence of broken time reversal symmetry, its band structure is marked by forced nodal lines at the Fermi edge. Moreover, this material hosts degenerate unconventional electronic quasiparticles. In particular, CrGe exhibits a sixfold degeneracy of fermions crossing within about 5 meV of the Fermi energy at the  $R$  point of the Brillouin zone.

## I. INTRODUCTION

Binary transition-metal monosilicides and monogermanides,  $TX$  with 50:50 composition ( $X = \text{Si}$  or  $\text{Ge}$  and  $T$  a  $3d$  transition metal), exist in the cubic noncentrosymmetric B20 lattice structure. Apart from the ordered intermetallic binary compounds, alloyed mixed series have also been investigated for a long time, but the interrelation of electronic and magnetic properties in these materials are not fully understood. In particular, for the semiconducting FeSi<sup>1</sup> and its peculiar paramagnetism, the role of electronic correlations, the absence of magnetic long-range order in its insulating ground state, and the nature of spin excitations in its paramagnetic state at finite temperatures are still not settled<sup>2,3</sup>.

MnSi has been used as a model system for studies on weak band ferromagnetism and the effect of spin fluctuations<sup>4</sup>. On the other hand, it was recognized early on as a prototypical chiral helimagnet<sup>5-7</sup>. The properties both of MnSi and FeGe illustrate the open questions about the relation between magnetism and electronic band-structure in these B20 materials. MnSi loses its helimagnetic order under a small hydrostatic pressure and becomes an anomalous metal with unconventional transport properties<sup>8</sup>. The magnetism in FeGe is much more stable under pressure, but above 19 GPa its electronic state appears to be semiconducting, when the magnetic moment on Fe collapses<sup>9</sup>.

The common feature of these materials is the cubic B20 structure ( $P2_13$ , #198) incorporating a helical arrangement of atoms along the  $\langle 111 \rangle$  crystal axes. As predicted by Dzyaloshinskii's theory of chiral magnetic ordering in noncentrosymmetric crystals<sup>10</sup>, the ferromagnetic long-range order both in MnSi and in FeGe is twisted into a

long-period spiral ground state with a fixed chirality<sup>5,6</sup>, which is an example for a Dzyaloshinskii spiral or texture. Microscopically, the twisting is caused by the relativistic Dzyaloshinskii-Moriya interaction<sup>11,12</sup>. However, the chiralities of the crystal structure and the magnetic order do not necessarily coincide. For example, in the  $\text{Mn}_{1-x}\text{Fe}_x\text{Ge}$  series, the magnetic chirality changes sign at  $x \approx 0.75$  without a structural change<sup>13</sup>. An overview concerning the properties of helimagnets can be found in Ref. [14].

Generally, in the germanide series the tendency for magnetic long-range order is stronger. Hence, FeGe is well described as a strong band ferromagnet<sup>15</sup>, but behaves similarly to MnSi as chiral helimagnet at ambient pressure<sup>16</sup>. Theoretically, chiral magnetic skyrmions as particle-like solitonic states had been predicted to exist in such chiral helimagnets for a long time, and the possibility to form thermodynamically stable condensates of these vortex- or swirl-like objects in the magnetic phase-diagram of chiral helimagnets was suggested<sup>17-19</sup>. After the experimental observation of such states<sup>20-22</sup>, the magnetism of B20 compounds has become a very active field of research.

MnGe, as isoelectronic counterpart to MnSi, is also a chiral helimagnet. It has the highest magnetic moment in the series of  $3d$  transition-metal germanides with B20 structure<sup>23</sup>. The magnetism in MnGe is complex with the possibility of spin-state transitions<sup>24</sup>, antiferromagnetic couplings<sup>25</sup>, and prominent magneto-elastic couplings<sup>26</sup>. The period of its spiral state is very short and has an anomalous field and temperature dependence, which is not expected for a Dzyaloshinskii spiral<sup>10</sup>. Kanazawa *et al.* have claimed the existence of a so-called “three-dimensional skyrmion state” at zero field in this

material<sup>23,27–29</sup>. However, the existence of such states is an open question, as these types of magnetic textures require a high density of magnetic hedgehog defects<sup>30</sup>. For  $\text{Mn}_{1-y}\text{Co}_y\text{Ge}$  and  $\text{Mn}_{1-y}\text{Rh}_y\text{Ge}$  alloy series, it has been argued that quenched disorder rather favors continuous undefected textures akin to twisted grain-boundary phases<sup>31</sup>. The remaining 3d transition-metal monosilicides with B20 structure NiSi, CoSi, and CrSi are described as paramagnetic or diamagnetic metals<sup>32,33</sup>. However, in the monosilicide alloy series, such as  $\text{Fe}_{1-x}\text{Co}_x\text{Si}$  or  $\text{Fe}_{1-x}\text{Mn}_x\text{Si}$ , magnetic long-range order and helimagnetism is found<sup>34</sup>.

CrGe is the only transition-metal germanide which readily adopts a B20 crystal structure<sup>35</sup>. Measurements of the magnetic susceptibility  $\chi$  revealed a Curie-Weiss-like behavior above 150 K with a sizeable effective moment of  $\mu_{eff} = 2.0\mu_B$  indicating large fluctuating Cr moments at high temperatures. In this respect, CrGe resembles FeSi at elevated temperatures. However, below 100 K, instead of increasing further, the magnetic susceptibility  $\chi(T)$  forms a broad maximum at about 60 K and merges below 20 K in a temperature-independent strongly enhanced Pauli susceptibility<sup>36</sup>. Accordingly, neutron-diffraction experiments showed no magnetic order down to 4.2 K<sup>37</sup>. Some susceptibility experiments indicated a small ordered magnetic moment in CrGe, but this was shown to arise from  $\text{Cr}_{11}\text{Ge}_{19}$  impurities<sup>38</sup>. Both the temperature dependence of the susceptibility and the resistivity of CrGe indicate its proximity to ferromagnetism<sup>39</sup>. Correspondingly, the Curie-Weiss-like behavior was explained by means of the paramagnon theory<sup>39–41</sup>. However, an onset of magnetic ordering has been found in the alloy series  $\text{Cr}_{1-y}\text{Mn}_y\text{Ge}$  for  $y > 0.06$  where first ferromagnetism and a reentrant chiral or helical magnetic glassy state have been observed<sup>42,43</sup>. Thus, CrGe appears to be close to a magnetically ordered or partially ordered state also under chemical substitution by another 3d metal, which again is similar to FeSi.

Interestingly, the band structures of the transition-metal germanides MnGe, FeGe, and CoGe were shown to be very similar<sup>44</sup>. The different valence-electron count leads only to a rigid band shift, with little change in the shape of the bands themselves<sup>44</sup>. Thus, we were encouraged to investigate CrGe, which possesses one 3d electron less than MnGe. Indeed, the band structures of CrGe and MnGe are very similar, as shown in Fig. 1. This poses the question why the B20 compound CrGe does not show magnetic order.

This question is crucial also to assess the possibility to identify specific features in the band structures of intermetallics with the noncentrosymmetric and nonsymmetrical cubic B20 structure. It has been recognized for a longer time that these systems have the potential to display topologically nontrivial band structures. For MnSi, it has been demonstrated that band degeneracies must occur at the boundary of the Brillouin zone (BZ). This enforces nodal rings for Fermi surface (FS) sheets in metallic systems<sup>45</sup>. Further special features in

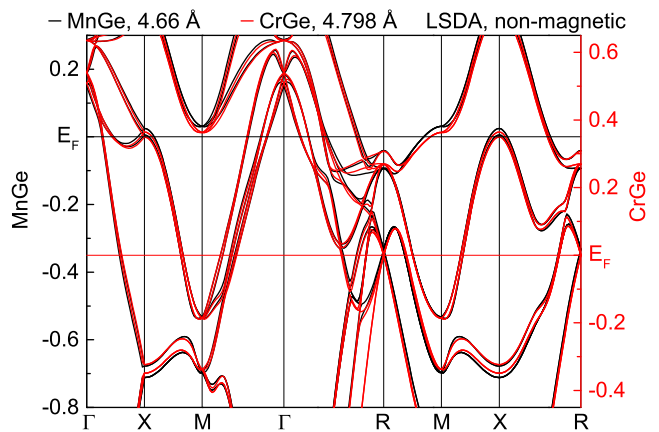


FIG. 1. Calculated band structures of CrGe and MnGe. In order to illustrate the similarities of the band structures, the MnGe band structure calculated for a reduced lattice parameter is shown, thus enhancing the band width.

the generic band structures of cubic crystals described by the  $P2_13$  space group have been uncovered, as unconventional multiply degenerate Weyl-like quasiparticle dispersions for electronic states, but also for other elementary excitations such as phonons<sup>46–49</sup>. Corresponding results from theory-based calculations and experiments have been reported for CoSi, RhSi, RhGe, and other systems<sup>47,48,50,51</sup>. However, these specific degeneracies of band dispersions in a B20 intermetallic can be shown to exist only if time-reversal symmetry remains unbroken, i. e., in the absence of magnetic ordering.

In this manuscript, we first present an experimental re-investigation of basic properties of CrGe, i. e., magnetic susceptibility, resistivity, and specific heat down to 1.8 K in high-quality single crystals. These data confirm CrGe as a paramagnetic metallic system with signatures of thermally excited spin fluctuations. Then, detailed measurements of the de Haas-van Alphen (dHvA) effect in CrGe are shown and compared to extensive band-structure calculations based on density-functional theory (DFT). Although bare DFT results predict a spin-polarized ground state, the dHvA data only agree with the band structure of a non-magnetic state. In order to assess the closeness to magnetic order theoretically, we use DFT+X calculations<sup>24,52</sup> to determine an exchange reduction factor  $\xi$  correctly describing the evolution of the magnetic moment for the substitution of Cr by Mn for the alloy series  $\text{Cr}_{1-y}\text{Mn}_y\text{Ge}$ . Finally, we compute the magnetic moment of CrGe under impact of negative and chemically induced pressures, (i) through lattice expansion or (ii) substitution of Ge by Sn or As, which leads to a lattice expansion or an increased band filling, respectively. The results show that the band structure of CrGe is very similar to MnGe, and that CrGe is close to a magnetic instability.

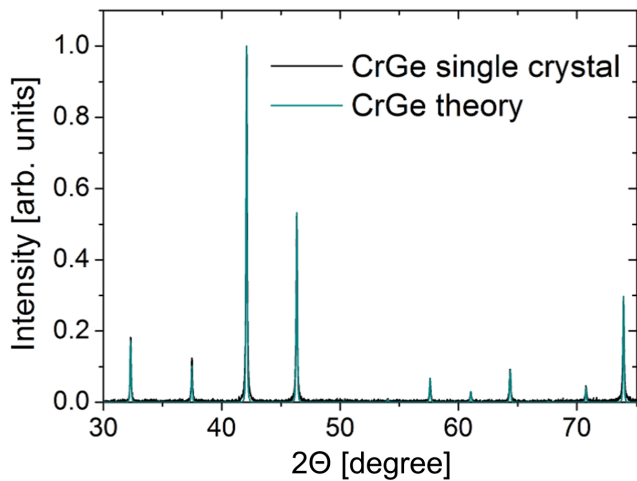


FIG. 2. Powder x-ray diffractogram of crushed single crystals (black), compared with a calculated spectrum for CrGe with B20 structure type (blue).

## II. EXPERIMENTS

### A. Synthesis

Based upon a report on crystal growth by chemical vapor transport in the system Cr/Ge<sup>53</sup>, we grew CrGe single crystals using this technique with iodine as transport agent. In a first step, we synthesized polycrystalline CrGe in an isothermal reaction of the elements chromium (powder, Alfa Aesar 99.996%) and germanium (powder, Alfa Aesar 99.999%) in the presence of iodine (Alfa Aesar 99.998%) at 875°C in evacuated fused silica tubes during 120 h. In a second step, CrGe single crystals with a volume of about 2 mm<sup>3</sup> each were grown by a chemical transport reaction in a temperature gradient from 875°C (source) to 925°C (sink), and a transport agent concentration of 1 mg/cm<sup>3</sup> iodine. Selected single crystals were characterized by energy-dispersive x-ray spectroscopy, x-ray powder diffraction, and oriented using x-ray single-crystal diffraction. These studies confirmed the single crystals to be cubic CrGe. No signature of impurity phases was found by x-ray diffraction, see Fig. 2. All peaks observed in powder x-ray diffractograms taken from crushed single crystals could be perfectly accounted for by the CrGe B20 phase (Fig. 2). We did not observe any evidence for an impurity phase. The extracted lattice parameter  $a = 4.796$  Å agrees very well with published data<sup>54</sup>.

### B. Magnetic susceptibility

The susceptibility determined in a commercial SQUID (Quantum Design) shows a Curie-Weiss behavior above 150 K, a broad maximum at about 60 K, and levels out in a temperature-independent Pauli-type susceptibility

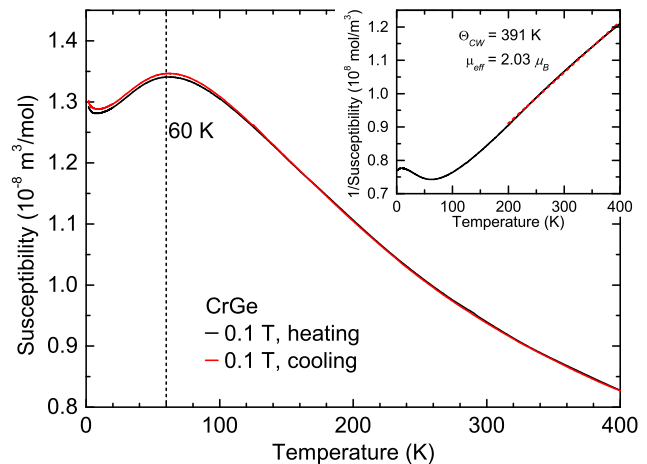


FIG. 3. Temperature dependence of the magnetic susceptibility of a CrGe single crystal plotted as  $\chi(T)$  vs.  $T$  (main) and  $1/\chi$  vs.  $T$  (inset). The very tiny difference between the heating and cooling curve is smaller than the accuracy of the experimental technique.

$\chi_0 = 1.257 \times 10^{-8}$  m<sup>3</sup>/mol below 20 K (Fig. 3). In contrast to previously published data, there is no evidence for a ferromagnetic (FM) component<sup>38</sup>, nor for an antiferromagnetic (AFM) transition<sup>36,39</sup>. Furthermore, the impurity-induced Curie-like increase at very low  $T$  is much smaller than in previous results reported for polycrystalline samples<sup>55</sup>. As a result, the broad anomaly at around 60 K is much better defined in the present results than in previous ones, providing additional support for CrGe being a nearly FM system and not an AFM one. The effective moment deduced from a Curie-Weiss fit above 200 K amounts to  $\mu_{eff} = 2.03 \mu_B$ , a value just in-between the values reported by [36] and [38], and a factor of about 1.4 larger than that reported in [55]. This fit results in a quite large negative Curie-Weiss temperature  $\Theta_{CW} = -391$  K, close to the value  $-400$  K reported in [38], but almost a factor of 2 larger than the values  $-260$  K and  $-204$  K reported in [36] and [39], respectively. This large negative  $\Theta_{CW}$  might indicate that CrGe is still at some distance from a FM state, or closer to an AFM than a FM state. The ratio between the low-temperature Pauli-like susceptibility  $\chi$  and the Sommerfeld coefficient  $\gamma$  (see below) results in an enhanced Sommerfeld-Wilson ratio  $R = \chi/\gamma \cdot \pi^2 k_B^2 / (\mu_0 \cdot \mu_{eff}^2) = 3$ , implying a significant amount of magnetic correlations. Here,  $k_B$  corresponds to the Boltzmann constant and  $\mu_0$  to the magnetic constant.

### C. Resistivity and specific heat

The temperature dependence of the resistivity,  $\rho(T)$ , and of the specific heat,  $C(T)$ , of a single crystal were measured in a commercial PPMS systems (Quantum Design) using standard setups. Because of the small size and

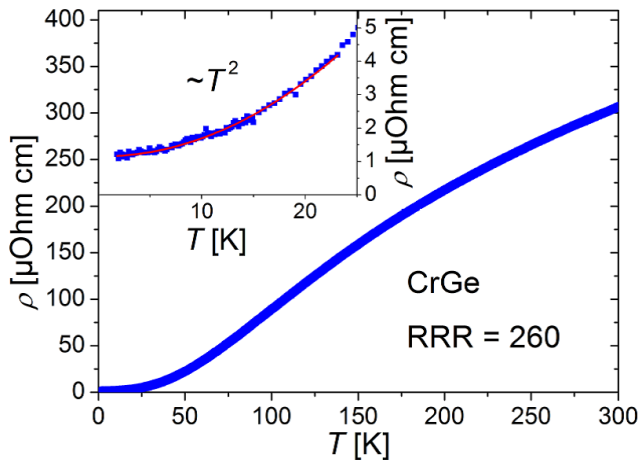


FIG. 4. Temperature dependence of the electrical resistivity of a CrGe single crystal.

the complex shape of the single crystal, a reliable determination of the geometry parameters entering the calculation of  $\rho$  was hampered. Therefore, the absolute values of  $\rho(T)$  shown in Fig. 4 might have a large error bar, but this does not affect the temperature dependence. The residual resistivity ratio  $RRR = \rho(300 \text{ K})/\rho(2 \text{ K}) = 260$  indicates an excellent crystallinity of the sample. The temperature dependence of  $\rho$  is in general that of a typical metal. At low temperatures ( $2 \text{ K} < T < 20 \text{ K}$ ) it follows a  $T^2$  dependence, which is likely a consequence of strong electron-electron scattering due to magnetic fluctuations. Such a  $T^2$  dependence was already noted in [39] and [55], but at higher temperatures than in our data.

The  $T$  dependence of the specific heat is shown in Fig. 5 as  $C(T)/T$  versus  $T$ . While above 10 K,  $C(T)$  is dominated by the phonon contribution, below 10 K,  $C(T)$  can be fitted with the standard  $C(T)/T = \gamma + \beta T^2$  expression. The fitted Sommerfeld coefficient,  $\gamma = 19 \text{ mJ}/(\text{mol K}^2)$ , is comparatively large for a metallic  $3d$  system, but can be well explained by a quite sizeable density of states (DOS) and a significant renormalization due to many-body interactions (see below). The coefficient  $\beta = 3.5 \cdot 10^{-5} \text{ J}/(\text{mol K}^4)$  of the phononic specific heat corresponds to a Debye temperature  $\Theta_D = 480 \text{ K}$ . The pronounced positive curvature in  $C(T)/T$  versus  $T^2$  above  $T = 10 \text{ K}$  is unusual for such a system where all components have a similar atomic mass. It might be due to additional magnetic fluctuations, but could also be due to some soft phonon modes. We are aware of only one published specific-heat study of CrGe<sup>56</sup>, which is furthermore limited to the  $T$  range  $T > 60 \text{ K}$ . At  $T = 60 \text{ K}$  and  $T = 160 \text{ K}$ , these data agree well with our result, but in between the published data are up to 20% below our results, resulting in an unrealistic, much too small temperature dependence at 60 K.

In summary, comparing the results we obtained on our single crystals with published data suggests that the present study provides a more consistent data set on the

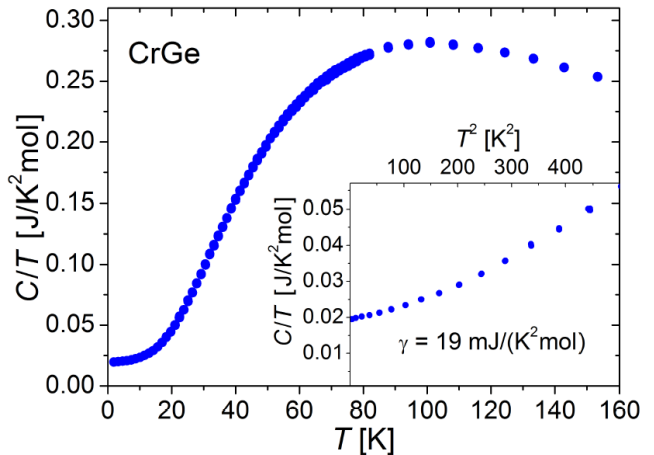


FIG. 5. Temperature dependence of the specific heat of a CrGe single crystal plotted as  $C(T)/T$  vs.  $T$  (main) and  $C(T)/T$  vs.  $T^2$  (inset).

basic physical properties of CrGe.

#### D. de Haas-van Alphen effect

Angle-dependent quantum-oscillation measurements were performed using capacitive torque magnetometry, employing  $50 \mu\text{m}$  thick CuBe cantilevers. Experiments were conducted in an 18-T superconducting magnet equipped with a dilution refrigerator at temperatures down to 40 mK. In addition, high-field measurements were performed at the HFML in Nijmegen in a 33 T resistive magnet equipped with a  $^3\text{He}$  cryostat at temperatures down to 330 mK. Figure 6(a) shows a typical as-measured torque signal for CrGe taken at an angle of  $\Theta_{0\bar{1}1} = 18^\circ$ , measured from the crystallographic [100] axis towards the [011] axis. Large quantum oscillations are clearly visible. By subtracting a non-oscillatory background and performing a Fourier transformation, we obtain the corresponding dHvA frequency spectrum shown in Fig. 6(b). Besides the dominant peak at  $F = 1.72 \text{ kT}$ , there is a multitude of other frequencies. These frequencies can be classified in two frequency groups, one at lower frequencies ranging from 1.6 to 3.6 kT and one at higher frequencies ranging from 6.4 to 7.1 kT. Due to the huge number of frequency maxima, a further division into frequency branches seemed futile.

Since there is no inversion symmetry in the B20 structure, dHvA frequencies are expected to be field-dependent<sup>57,58</sup> [see Supplementary Material (SM) for further information<sup>59</sup>]. Especially in the high-frequency group of Fig. 6(b), the frequency peaks are wider than the strongest peak at 1.72 kT. A separate analysis for different field ranges indeed shows changing frequencies (see SM<sup>59</sup>). In order to obtain frequencies closer to their zero-field value, we chose a low-field range ( $\mu_0 H = 10 - 18 \text{ T}$ ) for our analysis. Figure 7(a) shows the resulting angular

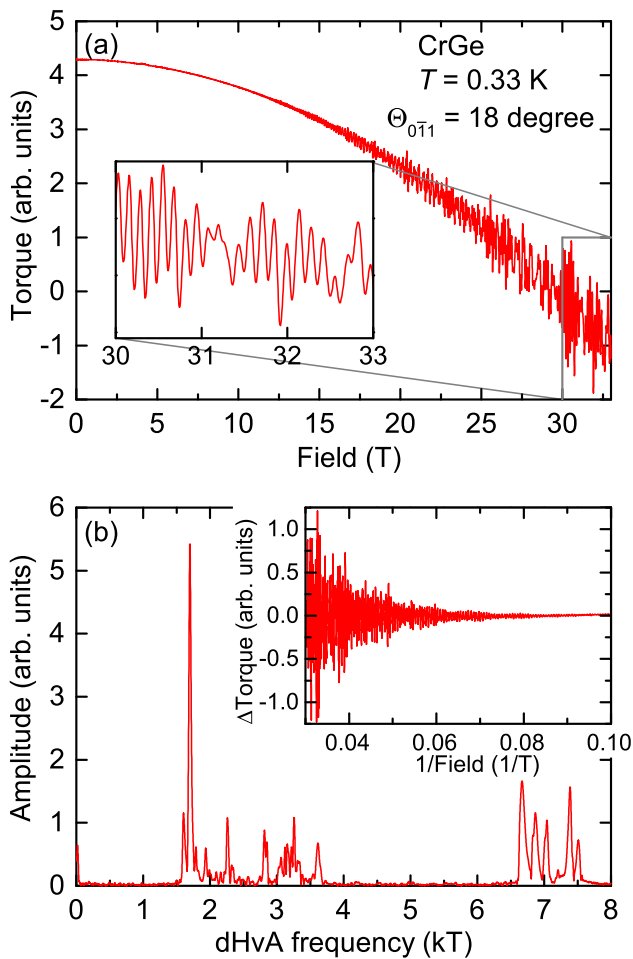


FIG. 6. (a) Example of a raw field-dependent torque signal of CrGe. Inset: Zoom on the data between 30 and 33 T. (b) Inset: Data shown in (a) after subtraction of a non-oscillatory background. Main panel: Corresponding dHvA frequency spectrum obtained by a Fourier transformation between 10 and 33 T.

dependence of the dHvA frequencies. For clarity, we did not include frequencies which are most likely higher harmonics. Since there are no obvious frequency branches, we decided to color-code the frequencies by their oscillation amplitudes. Usually, frequency maxima arising from fundamental frequencies of extremal dHvA orbits have a larger amplitude than those resulting from effects such as magnetic breakdown, magnetic interaction, or higher harmonics. Thus, the classification by amplitudes may help to identify true fundamental frequencies. We will discuss the angular dependence in more detail together with the calculated frequencies in Sec. III.

Figure 7(b) shows the temperature dependence of the Fourier spectrum, measured at the same angle as the data shown in Fig. 6. The oscillation amplitudes clearly decrease as the temperature increases from 0.33 to 1.17 K. As described by the Lifshitz-Kosevich formula, this reduction in amplitudes is proportional to  $x/\sinh x$ , where

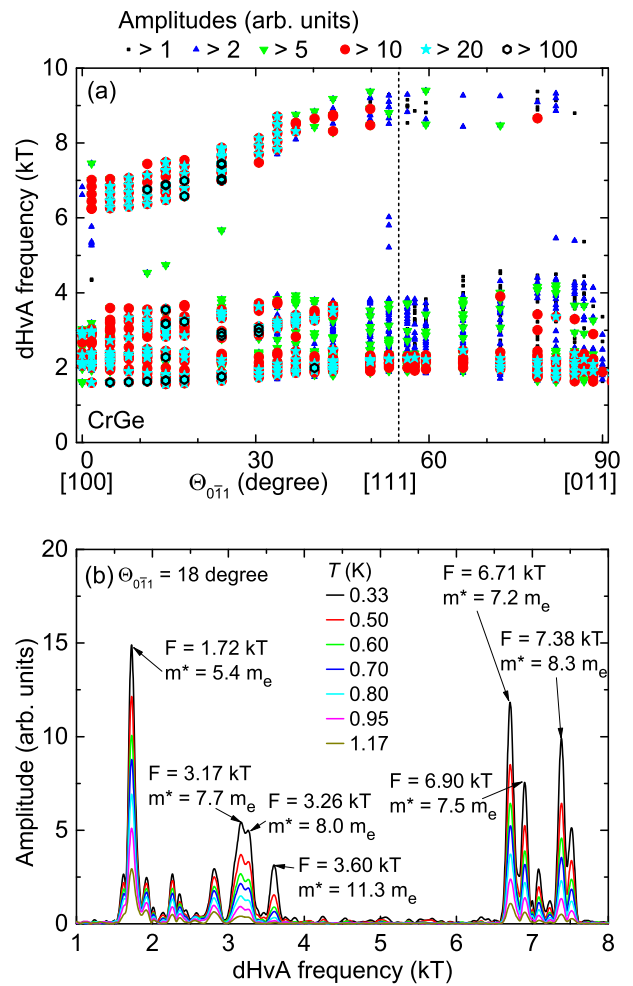


FIG. 7. (a) Angular dependence of the dHvA oscillation frequencies obtained from Fourier transformation in the range 10 – 18 T. Larger symbol sizes indicate larger amplitudes. (b) Temperature dependence of the frequency spectrum measured at  $\Theta_{0\bar{1}1} = 18^\circ$ , analyzed in the field range 20 – 33 T. The effective masses stated in the graph were obtained by fitting the Lifshitz-Kosevich formula to the temperature dependence of the oscillation amplitudes.

$x = \alpha T m^* / B$  and  $\alpha = 14.69 \text{ T/K}^{60}$ . Here,  $m^*$  represents the effective mass given in multiples of the free electron mass. By fitting this formula to the temperature dependence of the amplitudes, we obtain  $m^*$  as a fit parameter. Consistent with the slightly elevated electronic specific-heat coefficient, we also obtain enhanced effective masses, ranging from 4.6 to 11.3  $m_e$ . All effective masses are summarized in Table I, together with calculated band masses.

### III. FERMI-SURFACE CALCULATIONS

In order to determine the FS sheets corresponding to the experimental dHvA frequencies, we conducted band-structure calculations for CrGe. We used the

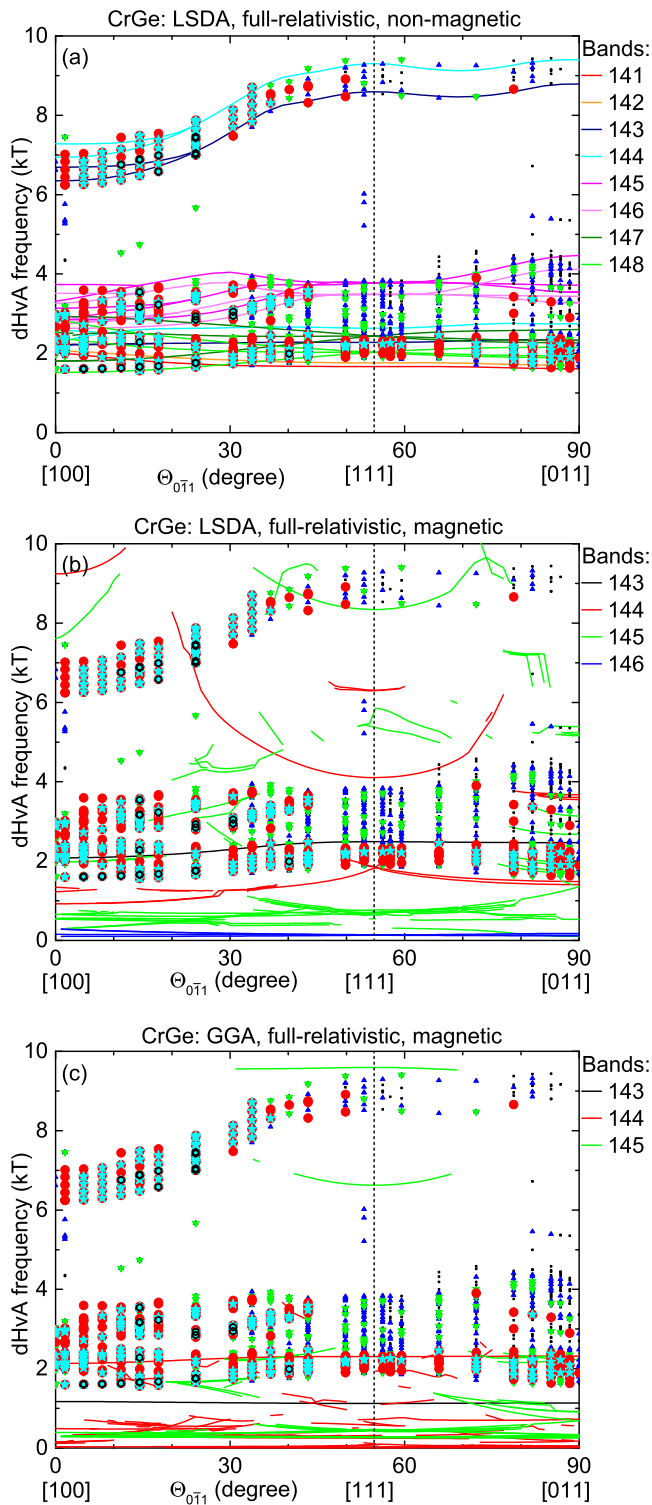


FIG. 8. Comparison of the experimental dHvA data (symbols) to calculated extremal FS cross-sections (lines) based on different assumptions: (a) LSDA and no magnetic ordering, (b) LSDA and magnetic ordering, and (c) GGA and magnetic ordering. Different colors of the lines represent the extremal FS orbits corresponding to different bands. The colors of the symbols are chosen identically to Fig. 7(a).

FPLO code<sup>61</sup> with a full-relativistic setting taking spin-orbit coupling (SOC) into account. To approximate the exchange and correlation potential, we used both the local spin density approximation (LSDA) of Perdew and Wang<sup>62</sup> and the generalized gradient approximation (GGA) by Perdew, Burke, and Ernzerhof<sup>63</sup>. For comparison, we used both a single-spin setting which suppresses magnetic ordering as well as a two-spin setting. The lattice parameter of  $a = 4.798 \text{ \AA}$  was taken from Ref. [54]. Optimizing the internal positional parameters of Cr and Ge yielded  $x_{\text{Cr}} = y_{\text{Cr}} = z_{\text{Cr}} = 0.1351$  and  $x_{\text{Ge}} = y_{\text{Ge}} = z_{\text{Ge}} = 0.8452$  for the non-magnetic LSDA case.  $x_{\text{Ge}}$  agrees perfectly with the value 0.847 deduced from neutron-scattering data, while  $x_{\text{Cr}}$  is slightly smaller than the reported experimental value  $x_{\text{Cr}} = 0.143$ <sup>37</sup>. Switching to GGA or to magnetic order before optimization leads to a change of less than 0.002 in the internal atomic position parameters. We used a  $20 \times 20 \times 20$   $k$  mesh for calculating the self-consistent density and a 32 times denser grid for extracting the extremal FS cross-sections.

Figure 8 shows the comparison of the angular dependences of the experimental dHvA frequencies with the calculated extremal FS cross-sections. Since GGA and LSDA yield virtually identical results for the non-magnetic setting, we only included the LSDA graph [Fig. 8(a)]. Obviously, both the magnetic calculations using LSDA [Fig. 8(b)] and GGA [Fig. 8(c)] disagree with the experimental data. On the other hand, there is excellent agreement of the non-magnetic calculations with the measured dHvA frequencies. The majority of the large-amplitude oscillations are reproduced by calculated extremal FS cross-sections. Vice versa, almost all the calculated cross-sections were found experimentally. Small deviations most likely arise from the aforementioned field-dependence of the dHvA frequencies. The calculated cross-sections of the two smallest FS sheets near  $B \parallel [111]$ , belonging to bands 141 and 142, are not reproduced by experimental dHvA frequencies. This is not surprising because torque magnetometry can only detect anisotropic FS sheets<sup>60</sup>. Since the calculated cross-sections for bands 141 and 142 barely change at all near the [111] direction, they are hardly observable for torque experiments.

The origin of the additional experimental frequencies not supported by calculations becomes clear when looking at the band structure and the corresponding FSs, shown in Fig. 9. In total, there are eight bands crossing the Fermi energy ( $E_F$ ). The nonsymmorphic and non-centrosymmetric  $P2_13$  structure causes a degeneracy of electronic bands on the BZ boundary, which is lifted elsewhere by SOC<sup>45</sup>. This enforces the presence of nodal lines, where bands, split by SOC, are degenerate, a feature of band structures in Weyl semimetals now termed “forced nodal lines”<sup>46,64</sup>. However, due to the low atomic numbers of Cr and Ge, this effect results in a rather small splitting of less than 40 meV on the high-symmetry lines in the BZ, shown in Fig. 9(a). Thus, the bands and

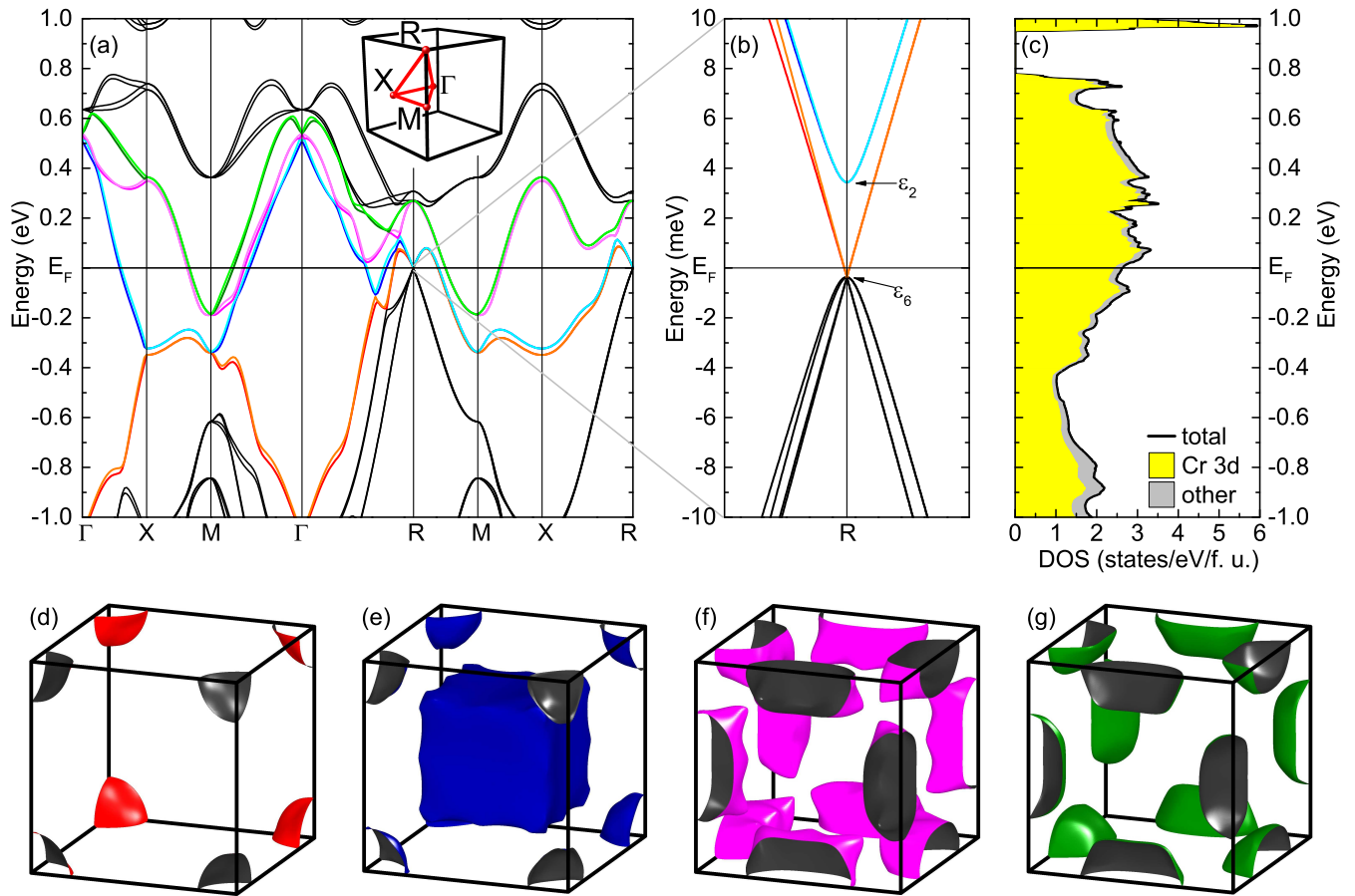


FIG. 9. (a) Calculated band structure of CrGe along high-symmetry axes of the BZ. Conduction bands are shown in the same color as their corresponding extremal FS cross-sections in Fig. 8(a). On the BZ boundary ( $R-M-X-R$ ), bands are pairwise degenerate. (b) Details of the band structure near  $R$ . (c) DOS near  $E_F$ . Yellow areas indicate contributions of Cr-3d orbitals. (d)-(g) Calculated FS sheets. Since the FSs of spin-split pairs of bands are very similar, we only show the surfaces of bands 141 (d), 143 (e), 145 (f), and 147 (g). The FS colors correspond to the band colors in (a). All FS sheets are shown in the SM<sup>59</sup>.

the corresponding FSs are almost identical. For that reason, we show the FSs corresponding to only one of each pair of such bands in Fig. 9(d)-(g) (see SM for images of all FSs<sup>59</sup>). As the spin splitting on the BZ boundary is zero, the FS sheets display closed loops with nodal lines, which also intersect at the edges of the BZ. Furthermore, the energy difference between separate pairs of bands on the line  $R-M$  amounts to only a few meV. Consequently, there are various degeneracies of multiple FS sheets and whole regions within the BZ, where FS sheets are either intersecting or very close to each other. This enables electrons to tunnel between different cyclotron orbits at sufficiently large magnetic fields, an effect called magnetic breakdown<sup>60</sup>. Therefore, many of the experimental data points lying between calculated cross-sections in Fig. 8(a) are most likely attributed to magnetic breakdown. The remaining outliers might be caused by the large number of frequencies with large amplitudes of oscillatory magnetization  $\tilde{M}(B)$ . In this situation, for a given external field  $H$ , multiple values of the internal field  $B = \mu_0[H + \sum \tilde{M}(B)]$  are possible, leading to

additional frequency peaks that are sums or differences of fundamental dHvA frequency peaks<sup>60</sup>. This effect is known as magnetic interaction and can be observed even in simple systems such as indium<sup>65</sup>. However, none of the frequencies produced by magnetic breakdown or interaction indicate additional extremal FS cross sections.

Interestingly, there is a sixfold degenerate crossing point at the  $R$  point close to  $E_F$ , with two more bands lying only a few meV above the crossing point, as shown in Fig. 9(b). While the crossing is symmetry-protected and hence independent of calculation parameters, its distance  $\varepsilon_6$  relative to  $E_F$  may slightly differ. To improve accuracy, we increased the density of the  $k$  mesh to  $40 \times 40 \times 40$ , doubling the number of  $k$  points for each dimension. We find values of  $\varepsilon_6 = -0.4$  meV (LSDA) and  $\varepsilon_6 = -4.2$  meV (GGA) for the sixfold crossing and  $\varepsilon_2 = 3.4$  meV (LSDA) and  $\varepsilon_2 = -0.5$  meV (GGA) for the two additional bands. A further refinement of the mesh density to  $96 \times 96 \times 96$  with LSDA yields values  $\varepsilon_6$  and  $\varepsilon_2$  that are about 1 meV larger than before. For all settings, the crossing points remain within  $\pm 5$  meV of

Experiment		FPLO calculation			$\lambda$
$F$ [kT]	$m^*$ [ $m_e$ ]	Band	$F$ [kT]	$m_b$ [ $m_e$ ]	$m^*/m_b - 1$
1.72	5.4	148	1.60	1.8	3.2
		141	1.78	1.3	
		147	1.90	1.8	
1.92	4.6	142	1.91	1.3	2.5
		2.01	5.6	148	
2.26	5.5	143	2.25	1.8	2.1
		2.36	5.6	148	
147	2.48			1.9	
144	2.62			2.0	
146	2.70			1.8	
147	2.83			2.5	
145	2.89			1.9	
146	2.95			2.3	
2.81	5.5	146	2.99	2.5	1.2
		145	3.20	2.5	
		145	3.23	2.6	
		146	3.61	3.1	
3.17	7.7	145	3.81	3.2	2.1
		145	3.20	2.5	
3.26	8.0	145	3.23	2.6	2.1
3.60	11.3	146	3.61	3.1	2.6
		145	3.81	3.2	
6.71	7.2	143	6.73	2.9	1.5
6.90	7.5	143	6.86	3.1	1.4
7.08	7.9				
7.23	7.7				
7.38	8.3	144	7.35	3.2	1.6
7.51	8.3	144	7.45	3.3	1.5

TABLE I. Experimental and calculated dHvA frequencies and effective masses of CrGe at the angle  $\Theta_{0\bar{1}1} = 18^\circ$ . The experimental values were taken in the field range between 20 and 33 T.

$E_F$  and the splitting  $\varepsilon_2 - \varepsilon_6 = 3.8(1)$  meV is constant. Note that the additional tiny FS sheets related to the bands crossing  $E_F$  near  $R$  correspond to dHvA frequencies smaller than 5 T, which are too small to be resolved in our experiments.

The large number of bands at  $E_F$  causes a fairly high DOS of 2.62 states/(eV·formula unit) [Fig. 9(c)]. More than 90% of the DOS derive from Cr-3d states. Using  $\gamma_{\text{calc}} = D(E_F)\pi^2 k_B^2/3$ , we calculate a Sommerfeld coefficient of  $\gamma_{\text{calc}} = 6.37$  mJ/(mol K<sup>2</sup>). Here,  $D(E_F)$  corresponds to the DOS at  $E_F$ . Comparing the calculated and the experimental value of  $\gamma = 19$  mJ/(mol K<sup>2</sup>) reveals a significant mass enhancement of  $\lambda = \gamma/\gamma_{\text{calc}} - 1 = 2.0$ . We also calculated the band masses  $m_b$  by taking the derivative  $dF/dE$ . For  $\Theta_{0\bar{1}1} = 18^\circ$ , all experimental and calculated frequencies and masses are shown in Table I. The field dependence of the experimental frequencies and the high number of frequencies renders a certain assignment between theory and experiment challenging. In Table I, we assigned the closest calculated frequency to the theoretical one, if their difference is smaller than 0.1 kT. Thus, we deduced mass enhancements of  $\lambda = 1.2 \dots 3.3$  for different bands with an average value of 2, in agreement with the value obtained from the electronic specific-heat coefficient. Altogether, the non-magnetic LSDA calculations yield an excellent description of the electronic structure of CrGe.

#### IV. DFT CALCULATIONS IN SEARCH OF SPIN-POLARIZED STATES

In this section, we used DFT calculations to assess how close CrGe may be to a spin-polarized or magnetically long-range ordered state.

First, we employ the GGA\*X method to investigate the alloy series  $\text{Cr}_{1-y}\text{Mn}_y\text{Ge}$  and compare to experimental data<sup>42</sup>. From these calculations, we obtain an exchange-functional reduction factor  $\xi$  which takes spin fluctuations into account, and use this value for further calculations. In the simplest approach, the expansion of the lattice leads to a spin-polarized state. We calculate the magnitude of expansion needed and a possible realization by Sn substitution of Ge. Finally, we study the impact of As substitution of Ge as an experimental route to achieve magnetic order.

##### A. Alloy series $\text{Cr}_{1-y}\text{Mn}_y\text{Ge}$

First, we analyze the substitution series  $\text{Cr}_{1-y}\text{Mn}_y\text{Ge}$ . Magnetization data of  $\text{Cr}_{1-y}\text{Mn}_y\text{Ge}$  evidence a step-like onset of the spin moment for  $y > 0.06$ , followed by a steep rise of the ordering temperature, and a strongly magnetic state in the limiting MnGe system<sup>24,42</sup>. However, our standard GGA calculations predict a magnetic ground state even for pure CrGe ( $y = 0$ ), in contrast to experimental data. Since CrGe is a nearly ferromagnetic metal, a calculated magnetic ground state indicates an overestimation of the tendency towards magnetic order rather than a contradiction to the non-magnetic ground state. This overestimation reflects a known trend of DFT calculations to prefer magnetic ground states in systems that are on the verge of magnetic order (see, for example, Ref. [66] and references therein). Microscopically, spin fluctuations may be responsible for a suppression of magnetic order. Here, we use a simple approach to account for spin-fluctuation effects through rescaling of the exchange functional introduced by Ortzen *et al.*<sup>52</sup>, which implements Moriya's spin-fluctuation theory for weak band magnetism into the spin-density-functional theory. The approach works through an effective rescaling of the exchange functional by a reduction factor  $\xi < 1$ . It has been dubbed LSDA\*X or GGA\*X method<sup>24</sup>. For small enough values of  $\xi$  the spin-polarization is quenched, eventually. This approach has been shown to allow for a detailed and quantitative calculation of the step-wise collapse of the spin-polarized states in MnGe under pressure<sup>24,26</sup>. In order to include the impact of doping on the electronic structure, we use the virtual-crystal approximation (VCA)<sup>67</sup> for  $\text{Cr}_{1-y}\text{Mn}_y\text{Ge}$ . Compared to mere rigid shifts of the bands, the VCA method incorporates the interaction of additional charge with the conduction bands, improving the quantitative agreement with experimental data, see also Ref. [68]. Thus, we were able to determine the impact of Mn substitution also for intermediate substitution levels  $y$ .

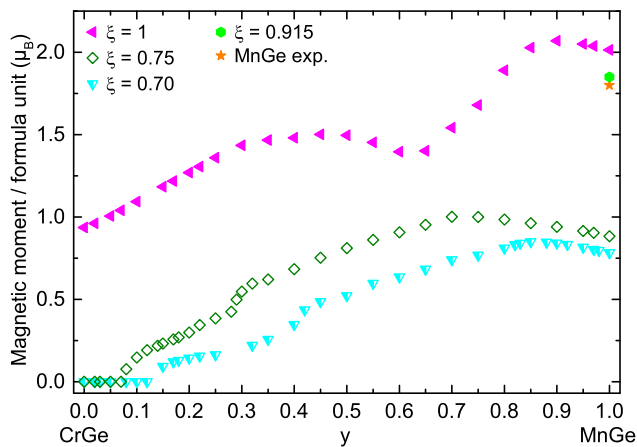


FIG. 10. GGA\*X calculations using the VCA for the alloy series  $\text{Cr}_{1-y}\text{Mn}_y\text{Ge}$  for different reduction factors  $\xi$ . The curve for  $\xi = 1$  corresponds to a standard GGA calculation. Experimental and theoretical spin moments ( $\xi = 0.915$ ) for pure MnGe are reproduced from Ref. [24].

For pure CrGe we find that the quenching of spin polarization is achieved only for a sizeable exchange reduction with  $\xi \leq 0.79$  in calculations using the GGA\*X functional (see SM for details on the GGA\*X calculations for pure CrGe<sup>59</sup>). Exemplary, we conducted GGA\*X calculations for  $\xi = 0.70$  and  $\xi = 0.75$ , which will both yield a paramagnetic ground state, and a standard GGA (i.e.  $\xi = 1$ ) for comparison. For all compositions, the cell parameters and atomic positions have been optimized in the calculations.

Fig. 10 shows the evolution of the net magnetic spin moment per formula unit (f.u.) with increasing Mn substitution derived from these calculations. Obviously, without accounting for the spin fluctuations, the standard GGA overestimates the spin polarization throughout the whole alloy series. For  $\xi = 0.75$ , we see a reasonable reproduction of the experimental data, providing the correct onset of magnetic order at  $y > 0.06$ , followed by a steeply rising moment and a maximum for  $y = 0.70$ , followed by a small decrease towards pure MnGe. A reduction factor of  $\xi = 0.70$ , however, yields magnetic order only for  $y > 0.125$ , hence overestimating the fluctuation effects. Thus, the GGA\*X with a reduction factor  $\xi = 0.75$  provides a realistic picture for small  $y < 0.30$  with an onset of a magnetic state for  $y > 0.06$ . For the range of larger Mn substitution,  $y > 0.30$ , a novel regime sets in, which tends towards an intermediate spin state in the GGA\*X calculations with  $\xi = 0.75$ . However, the limiting high-spin (HS) state in MnGe is reproduced in the calculations only by a minor reduction  $\xi = 0.915$ <sup>24</sup>. This suggests that the spin-fluctuation effects should be particularly strong in pure and Mn-substituted CrGe, but they have reduced importance for the magnetic state in MnGe.

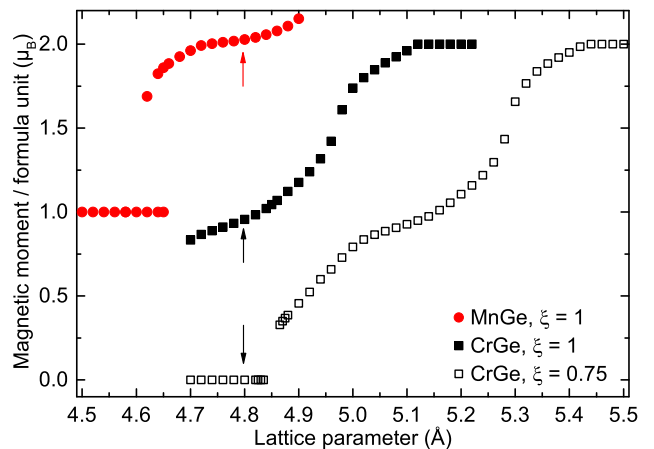


FIG. 11. Magnetic moments of CrGe and MnGe for different lattice parameters, calculated by GGA ( $\xi = 1$ ) and, for CrGe, also by GGA\*X ( $\xi = 0.75$ ). For a few lattice parameters, there are two (meta)stable magnetic ground states of MnGe. Arrows indicate the experimental ambient-pressure lattice parameters of CrGe and MnGe.

## B. Negative pressure

In MnGe, a HS state can be tuned into a low-spin (LS) state by the application of pressure<sup>24</sup>. Band-structure calculations for MnGe reproduce this behavior and indicate that both states can coexist in a narrow range of lattice parameters<sup>24,44</sup>. In general, increasing the lattice parameter of a compound reduces the overlap of the  $3d$  orbitals of neighboring atoms. Thus,  $3d$  bands become flatter and magnetic order is favored. In CrGe, the proximity to magnetic order, implied both by experimental data and our band-structure calculations, suggests that a small lattice expansion might lead to magnetic order. Thus, we were motivated to investigate whether CrGe switches into a magnetically ordered state by applying negative (chemically induced) pressure. Given that SOC leads only to very small effects in CrGe, we proceed with scalar-relativistic calculations, enabling us to conduct fixed spin-moment calculations with FPLO (see SM<sup>59</sup>). Again, we used both LSDA and GGA and compared the results. Since the MnGe calculations in Ref. [44] used a different code, we conducted similar calculations in order to improve the comparability to our CrGe results. Our calculations for MnGe are based on the  $P2_13$  structure, identical to the structure of CrGe, which can be obtained for MnGe by carefully controlling the crystal-growth conditions<sup>69</sup>. The MnGe lattice parameter of  $a = 4.797 \text{ \AA}$  was taken from Ref. [44] and internal atomic positions were optimized.

Figure 11 shows the results of the lattice-constant-dependent magnetic-moment calculations using GGA. The results obtained using LSDA are very similar, but shifted towards slightly higher lattice parameters. Therefore, we only discuss the GGA results in detail, whereas LSDA results can be found in the SM, Fig. S5(f)<sup>59</sup>. For

MnGe, we obtained results virtually identical to those reported in Ref. [44]. In the range of  $4.62 \text{ \AA} < a < 4.65 \text{ \AA}$ , the HS and LS configurations coexist. Below (above) this range, only the LS (HS) configuration is stable. The coexistence of both spin states in MnGe is confirmed by fixed-spin-moment calculations (see the SM, Fig. S5<sup>59</sup>). For the lattice parameters we considered, the moment per f. u. of the LS state is constant at  $1 \mu_B$ . However, the moment per f. u. of the HS state continuously increases from  $1.7 \mu_B$  at  $a = 4.62 \text{ \AA}$  to  $2.2 \mu_B$  at  $a = 4.90 \text{ \AA}$ . For the experimental MnGe lattice parameter of  $a = 4.797 \text{ \AA}$ , we obtain  $2.0 \mu_B$ , roughly consistent with an earlier experimental value of  $2.3(5) \mu_B$ <sup>27</sup>, but in better agreement with the newer experimental value of  $1.8(1) \mu_B$ <sup>24</sup>.

The general trend of increasing magnetic moment with increasing lattice parameter is also observed for standard GGA calculations for CrGe, as can be seen in Fig. 11. However, the impact of spin fluctuations in CrGe is much larger than in MnGe, leading to an overestimation of the magnetic moment. Using the GGA\*X method with  $\xi = 0.75$ , the calculated moment drastically reduces for all  $a$  and magnetic order completely disappears for  $a < 4.865 \text{ \AA}$ . We note that the GGA\*X data resemble the standard GGA data, shifted by  $0.32 \text{ \AA}$  to larger values. For both GGA and GGA\*X, the CrGe moment increases less abruptly and there are no distinct LS or HS states and no coexistence of two spin states for any lattice parameter, in contrast to MnGe. Instead of stable LS and HS states, there are regions with smaller and larger slope in the  $M(a)$  diagram. Only for large expansions, the moment per f. u. saturates at a value of  $2 \mu_B$  at  $a = 5.12 \text{ \AA}$  and  $a = 5.44 \text{ \AA}$  for GGA and GGA\*X, respectively. Considering GGA\*X more adequate to reflect the magnetic behavior of CrGe, our calculations predict that a lattice expansion beyond  $a = 4.865 \text{ \AA}$  will induce magnetic order in CrGe, and a further expansion will continuously increase the magnetic moment.

### C. Chemical substitution for Ge

In the next step, we investigate whether substituting Ge by larger Sn atoms suffices to provide the lattice expansion required for magnetic order. The lattice parameters of the resulting  $\text{CrGe}_{1-x}\text{Sn}_x$  could be linearly interpolated between the end members CrGe and CrSn, according to Vegard's law. However, to the best of our knowledge, the compound CrSn has not been synthesized yet. Therefore, we determined the lattice parameter of the hypothetical  $P2_13$ -CrSn compound by DFT calculations.

Generally, DFT codes provide limited accuracy for calculating ground-state lattice parameters<sup>70,71</sup>. Assuming that this offset is similar for similar materials, we calculated the lattice parameters for CrGe and CrSn, using both LSDA and GGA. Our calculations consistently yield a lattice expansion of 8.0% (LSDA) and 8.2% (GGA) when replacing Ge by Sn (for details, see the SM<sup>59</sup>). Thus, we

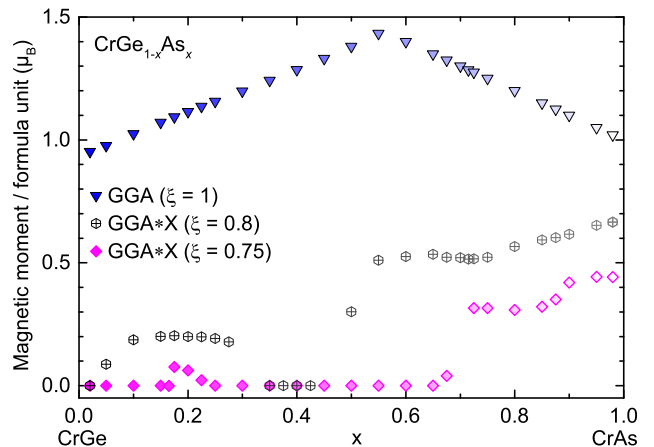


FIG. 12. Magnetic moment for different As contents in  $\text{CrGe}_{1-x}\text{As}_x$ , calculated both with GGA and GGA\*X. The fading symbol color for increasing  $x$  stresses a decreasing likelihood of a stable  $P2_13$  structure.

deduce that a putative  $P2_13$ -CrSn compound would have a lattice parameter about 8.1% larger than in CrGe. This corresponds to a lattice parameter of  $a = 5.187 \text{ \AA}$  for CrSn. Assuming a linear dependence  $a(x)$ , we estimate a Sn fraction of  $x = 0.17$  necessary to achieve  $a = 4.865 \text{ \AA}$ , the calculated onset value of magnetic order. However, the disorder in the  $\text{CrGe}_{1-x}\text{Sn}_x$  series caused by substitution leads to a smearing of the bands, which further suppresses magnetic order and which may influence the spin fluctuations as well. Consequently, the minimum value of  $x$  leading to magnetic order might deviate and requires an experimental investigation of the  $\text{CrGe}_{1-x}\text{Sn}_x$  series. For the limit of large  $x$ , we conducted GGA\*X calculations for CrSn with the same value of  $\xi = 0.75$  (not shown), yielding results virtually identical to those obtained for CrGe shown in Fig. 11. Hence, we deduce a maximum moment per f. u. of  $1.1 \mu_B$  for the putative  $P2_13$ -CrSn.

Considering that MnGe possesses one additional electron as compared to CrGe, we investigated the impact of adding an electron on the Ge site by As substitution. For that, we conducted calculations for  $\text{CrGe}_{1-x}\text{As}_x$  using the VCA<sup>67</sup>. For all  $x$ , we assumed that the  $P2_13$  crystal structure remains valid and used optimized lattice parameters. Note, however, that CrAs orders helimagnetically in its ground state crystal structure  $Pnma$ <sup>72</sup>, whereas the  $P2_13$  structure is only predicted to exist at high pressures<sup>73</sup>. Hence, it is difficult to estimate the maximum  $x$  for which  $\text{CrGe}_{1-x}\text{As}_x$  would actually be stable in the  $P2_13$  structure.

The calculated substitution dependence of the magnetic moment of  $\text{CrGe}_{1-x}\text{As}_x$  is shown in Fig. 12. Upon increasing the As content, the moment per f. u. calculated by standard GGA peaks at  $1.4 \mu_B$  at  $x \approx 0.55$ , and then decreases to  $1 \mu_B$  for pure CrAs. For standard LSDA, we find a similar behavior, but a smaller peak moment of  $1.1 \mu_B$  at  $x \approx 0.8$  (see SM<sup>59</sup>). Employing the GGA\*X

method with  $\xi = 0.75$  suppresses magnetic order. Sizeable magnetic moments set in for  $x > 0.65$  with a peak value of only about  $0.45 \mu_B$  at  $x = 0.95$ . However, the GGA\*X calculations find a small region with weak spin polarization in the range  $0.15 < x < 0.3$ , depending on the value of  $\xi$ . This may suggest that substitution of Ge by As (or by the isoelectronic ions Sb and P) may lead either to stronger spin-fluctuation effects or even magnetic ordering.

## V. SUMMARY AND CONCLUSIONS

In summary, we performed an investigation of the electronic properties of CrGe. First, through experimental re-investigation of basic thermodynamic and resistivity data, we ascertain that this system has a metallic paramagnetic ground state, although spin fluctuations seem to play an important role as displayed in the peak of the magnetic susceptibility. Then, we investigated in detail the band structure and Fermi surface of CrGe by combining band-structure calculations using DFT and dHvA measurements. Previous experimental data of CrGe describe a paramagnetic ground state which is close to ferromagnetic order<sup>39</sup>. Indeed, our dHvA measurements yield an agreement with calculations only for the non-magnetic case. As expected from the low atomic numbers of Cr and Ge, SOC leads to a small band splitting, which amounts to less than 40 meV on the high-symmetry lines of the BZ. However, even small SOC in the noncentrosymmetric crystal structure of CrGe should result in a chiral helimagnetic long-range order as the Dzyaloshinskii-Moriya interaction is the leading effect and only higher-order anisotropies could suppress the formation of a twisted non-collinear state.

Experimentally, the onset of magnetic ordering has been found in the alloy series  $\text{Cr}_{1-y}\text{Mn}_y\text{Ge}$  for  $y > 0.06$ , where first ferromagnetism and a reentrant chiral or helical magnetic glassy state has been observed<sup>42,43</sup>. From our DFT calculations such an onset of stable magnetic moments in this alloy series is plausible. The observed glassy state may signal either frustrated magnetic couplings, including antiferromagnetic exchange as also suggested for  $\text{MnGe}$ <sup>25</sup>, or the effect of quenched random anisotropy disorder on a chiral helimagnetic states, as in  $\text{Mn}_{1-y}\text{Co}_y\text{Ge}$  or  $\text{Mn}_{1-y}\text{Rh}_y\text{Ge}$ <sup>31</sup>.

Motivated by the similarities of the band structures of CrGe and MnGe, we conducted further calculations to investigate the relation of the magnetic moment of CrGe with its lattice parameter. Since there is one  $3d$  electron less in CrGe than in MnGe, a reduced tendency towards magnetic ordering is expected. However, standard DFT calculations do not take spin fluctuations into account, predicting a magnetic ground state for CrGe, in contrast to experiments<sup>39</sup>. For the  $\text{Cr}_{1-y}\text{Mn}_y\text{Ge}$  series, we used the GGA\*X approach to incorporate the impact of spin fluctuations. On the Cr-rich side, a reduction factor of  $\xi = 0.75$  reasonably reproduces the experimen-

tally confirmed onset of magnetic order at  $y > 0.06$ <sup>42</sup>. For pure MnGe,  $\xi = 0.915$  gives a correct value for the magnetization<sup>24</sup>, evidencing a weaker influence of spin fluctuation of the Mn-rich side. Using GGA\*X with  $\xi = 0.75$  for further calculations, we find an onset of magnetic order when expanding the CrGe lattice beyond  $a = 4.865 \text{ \AA}$  and a continuous increase of the total moment per f. u. up to a saturation of  $2 \mu_B$  at  $a = 5.44 \text{ \AA}$ . Unlike in MnGe, there is no sharp transition and no coexistence of LS and HS states for any lattice parameter.

We also calculated the impact of Sn and As substitution on the Ge site, assuming the  $P2_13$  structure remains stable. The isoelectronic substitution of Ge by larger Sn atoms increases the lattice parameter up to 8.1% to  $a = 5.187 \text{ \AA}$  for pure CrSn. Hence, using Vegard's law, a Sn fraction of  $x > 0.17$  is necessary to induce magnetic order in  $\text{CrGe}_{1-x}\text{Sn}_x$  by lattice expansion. However, since disorder-induced band smearing decreases the tendency to magnetic order, this value is rather a lower bound. In the  $\text{CrGe}_{1-x}\text{As}_x$  series, electron doping by partially substituting Ge by As induces magnetic order at a rather large value of  $x > 0.65$ , again assuming a stable  $P2_13$  structure and neglecting band-smearing effects. Additionally, our calculations suggest a small region of weak spin polarization around  $x = 0.2$ . Since for both  $\text{CrGe}_{1-x}\text{Sn}_x$  and  $\text{CrGe}_{1-x}\text{As}_x$ , the stability of the  $P2_13$  phase is unknown, further experimental research is necessary to explore the possibilities to induce helimagnetic order or even a skyrmion-lattice ground state in CrGe by substitution.

Our investigation thus provides two key facts on the band structure and electronic states in CrGe. First, time-reversal symmetry is preserved, although the paramagnetic ground state bears large spin-fluctuation effects. Second, the detailed structure of the FS sheets is reasonably well described by the non-spin-polarized band structure from DFT. CrGe has several interesting band-structure features that may be investigated in more detail in future. As there are several FS sheets cutting the BZ boundary, the electronic bands evaluated including SOC have several forced nodal lines at the Fermi energy. These specific features of the band structure cannot be resolved in the dHvA data, but may be responsible for the indications of magnetic breakdown. Moreover, the band structure shows several of the expected multiple degeneracy points with Weyl-like quasiparticle dispersion. Most prominent is a sixfold degenerate crossing point of bands at the  $R$  point close to  $E_F$ , see Fig. 9(b). In this respect, CrGe is a Weyl semi-metal with unconventional quasiparticles.

In conclusion, the intermetallic CrGe has a paramagnetic metallic ground state. The thermal properties at higher temperatures suggest strong spin fluctuations. In fact, strong renormalization effects are evidenced by enhanced effective carrier masses, ranging from 4.6 to  $11.3 m_e$ . GGA\*X calculations reproduce the paramagnetism in CrGe and the appearance of magnetic order in  $\text{Cr}_{1-y}\text{Mn}_y\text{Ge}$ . Moreover, Sn or As substitution on the

Ge site are predicted to induce magnetic order by lattice expansion or electron doping, respectively, but a high-spin state of Cr can be ruled out. Both because of the instability of the B20 structure and the comparatively weak tendency of Cr towards a magnetic state, an experimental verification is required. The proximity to a magnetic long-range order or at least a stable localized magnetic moment is a common feature of CrGe and the insulating anomalous paramagnetism of FeSi. Therefore, further experiments on CrGe may be required to understand the spin-fluctuation effects. On the other hand, the special topology of the CrGe band structure in absence

of magnetic order may give rise to anomalous transport properties and the topologically nontrivial band structure may be discernible by surface-sensitive probes.

## VI. ACKNOWLEDGMENTS

We acknowledge the support by HLD at HZDR and HFML-RU/FOM, which are both members of the European Magnetic Field Laboratory (EMFL), and the ANR-DFG grant “Fermi-NESt” (GE 602/4-1 and WO444/13-1). K. G. and K. W. acknowledge support from the DFG within GRK 1621.

- 
- \* j.klotz@hzdr.de  
 † Present address: Department of Physics, University of Warwick, Coventry, CV4 7AL, United Kingdom  
 ‡ Helge.Rosner@cpfs.mpg.de
- <sup>1</sup> V. Jaccarino, G. Wertheim, J. Wernick, L. R. Walker, and S. Aarj, Phys. Rev. **160**, 476 (1967).
  - <sup>2</sup> S. Paschen, E. Felder, M. A. Chernikov, L. Degiorgi, H. Schwer, H. R. Ott, D. P. Young, J. L. Sarrao, and Z. Fisk, Phys. Rev. B **56**, 12916 (1997).
  - <sup>3</sup> S. Khmelevskiy, G. Kresse, and P. Mohn, Phys. Rev. B **98**, 125205 (2018).
  - <sup>4</sup> T. Moriya, *Spin fluctuations in itinerant electron magnetism*, Vol. 56 (Springer Science & Business Media, 2012).
  - <sup>5</sup> P. Bak and M. H. Jensen, J. Phys. C: Solid State Physics **13**, L881 (1980).
  - <sup>6</sup> O. Nakanishi, A. Yanase, A. Hasegawa, and M. Kataoka, Solid State Commun. **35**, 995 (1980).
  - <sup>7</sup> G. Shirane, R. Cowley, C. Majkrzak, J. B. Sokoloff, B. Pagonis, C. H. Perry, and Y. Ishikawa, Phys. Rev. B **28**, 6251 (1983).
  - <sup>8</sup> J. Thompson, Z. Fisk, and G. Lonzarich, Physica B **161**, 317 (1989).
  - <sup>9</sup> P. Pedrazzini, H. Wilhelm, D. Jaccard, T. Jarlborg, M. Schmidt, M. Hanfland, L. Akselrud, H. Q. Yuan, U. Schwarz, Y. Grin, and F. Steglich, Phys. Rev. Lett. **98**, 047204 (2007).
  - <sup>10</sup> I. Dzyaloshinskii, Sov. Phys. JETP **19**, 960 (1964).
  - <sup>11</sup> I. Dzyaloshinsky, J. Phys. Chem. Solids **4**, 241 (1958).
  - <sup>12</sup> T. Moriya, Phys. Rev. **120**, 91 (1960).
  - <sup>13</sup> S. V. Grigoriev, N. M. Potapova, S.-A. Siegfried, V. A. Dyadkin, E. V. Moskvina, V. Dmitriev, D. Menzel, C. D. Dewhurst, D. Chernyshov, R. A. Sadykov, L. N. Fomicheva, and A. V. Tsvyashchenko, Phys. Rev. Lett. **110**, 207201 (2013).
  - <sup>14</sup> N. Nagaosa and Y. Tokura, Nat. Nanotechnol. **8**, 899 (2013).
  - <sup>15</sup> M. Neef, K. Doll, and G. Zwirnagl, Phys. Rev. B **80**, 035122 (2009).
  - <sup>16</sup> B. Lebech, J. Bernhard, and T. Freltoft, J. Phys.: Condensed Matter **1**, 6105 (1989).
  - <sup>17</sup> A. N. Bogdanov and D. A. Yablonskii, Sov. Phys. JETP **68**, 101 (1989).
  - <sup>18</sup> A. Bogdanov and A. Hubert, J. Magn. Magn. Mater. **138**, 255 (1994).
  - <sup>19</sup> A. Bogdanov, U. Rössler, and C. Pfleiderer, Physica B **359**, 1162 (2005).
  - <sup>20</sup> S. Mühlbauer, B. Binz, F. Jonietz, C. Pfleiderer, A. Rosch, A. Neubauer, R. Georgii, and P. Böni, Science **323**, 915 (2009).
  - <sup>21</sup> C. Pappas, E. Lelièvre-Berna, P. Falus, P. M. Bentley, E. Moskvina, S. Grigoriev, P. Fouquet, and B. Farago, Phys. Rev. Lett. **102**, 197202 (2009).
  - <sup>22</sup> X. Z. Yu, Y. Onose, N. Kanazawa, J. H. Park, J. H. Han, Y. Matsui, N. Nagaosa, and Y. Tokura, Nature **465**, 901 (2010).
  - <sup>23</sup> N. Kanazawa, Y. Onose, T. Arima, D. Okuyama, K. Ohoyama, S. Wakimoto, K. Kakurai, S. Ishiwata, and Y. Tokura, Phys. Rev. Lett. **106**, 156603 (2011).
  - <sup>24</sup> M. Deutsch, O. Makarova, T. C. Hansen, M. Fernandez-Diaz, V. Sidorov, A. Tsvyashchenko, L. Fomicheva, F. Porcher, S. Petit, K. Koepf, *et al.*, Phys. Rev. B **89**, 180407 (2014).
  - <sup>25</sup> V. A. Chizhikov and V. E. Dmitrienko, Phys. Rev. B **88**, 214402 (2013).
  - <sup>26</sup> N. Martin, M. Deutsch, J.-P. Itie, J.-P. Rueff, U. K. Rössler, K. Koepf, L. N. Fomicheva, A. V. Tsvyashchenko, and I. Mirebeau, Phys. Rev. B **93**, 214404 (2016).
  - <sup>27</sup> O. L. Makarova, A. V. Tsvyashchenko, G. Andre, F. Porcher, L. N. Fomicheva, N. Rey, and I. Mirebeau, Phys. Rev. B **85**, 205205 (2012).
  - <sup>28</sup> N. Kanazawa, J.-H. Kim, D. S. Inosov, J. S. White, N. Ege-tenmeyer, J. L. Gavilano, S. Ishiwata, Y. Onose, T. Arima, B. Keimer, and Y. Tokura, Phys. Rev. B **86**, 134425 (2012).
  - <sup>29</sup> T. Tanigaki, K. Shibata, N. Kanazawa, X. Yu, Y. Onose, H. S. Park, D. Shindo, and Y. Tokura, Nano Lett. **15**, 5438 (2015).
  - <sup>30</sup> N. Kanazawa, Y. Nii, X.-X. Zhang, A. Mishchenko, G. De Filippis, F. Kagawa, Y. Iwasa, N. Nagaosa, and Y. Tokura, Nature Commun. **7**, 11622 (2016).
  - <sup>31</sup> N. Martin, M. Deutsch, G. Chaboussant, F. Damay, P. Bonville, L. N. Fomicheva, A. V. Tsvyashchenko, U. K. Rössler, and I. Mirebeau, Phys. Rev. B **96**, 020413 (2017).
  - <sup>32</sup> D. Van der Marel, A. Damascelli, K. Schulte, and A. Menovsky, Physica B **244**, 138 (1998).
  - <sup>33</sup> V. Narozhnyi and V. Krasnorussky, J. Exp. Theor. Phys. **116**, 780 (2013).

- <sup>34</sup> J. Beille, J. Voiron, and M. Roth, *Solid State Commun.* **47**, 399 (1983).
- <sup>35</sup> H. J. Wallbaum, *Naturwissenschaften* **32**, 76 (1944).
- <sup>36</sup> K. Yasukōchi, K. Yamagiwa, Y. Kuwasawa, and K. Sekizawa, *J. Phys. Soc. Jpn.* **21**, 557 (1966).
- <sup>37</sup> M. Kolenda, J. Leciejewicz, and A. Szytuła, *Phys. Status Solidi B* **57**, K107 (1973).
- <sup>38</sup> M. Kolenda, J. Stoch, and A. Szytuła, *J. Magn. Magn. Mater.* **20**, 99 (1980).
- <sup>39</sup> T. Sato and M. Sakata, *J. Phys. Soc. Jpn.* **52**, 1807 (1983).
- <sup>40</sup> R. Jullien, M. T. Béal-Monod, and B. Coqblin, *Phys. Rev. B* **9**, 1441 (1974).
- <sup>41</sup> M. T. Béal-Monod and J. M. Lawrence, *Phys. Rev. B* **21**, 5400 (1980).
- <sup>42</sup> T. Sato, J. Kozu, K. Oshiden, T. Nemoto, E. Ohta, M. Sakata, T. Goto, and T. Sakakibara, *J. Phys. Soc. Jpn.* **57**, 639 (1988).
- <sup>43</sup> T. Sato, T. Ando, T. Oku, and M. Furusaka, *Phys. Rev. B* **49**, 11864 (1994).
- <sup>44</sup> J. F. DiTusa, S. B. Zhang, K. Yamaura, Y. Xiong, J. C. Prestigiacomo, B. W. Fulfer, P. W. Adams, M. I. Brickson, D. A. Browne, C. Capan, Z. Fisk, and J. Y. Chan, *Phys. Rev. B* **90**, 144404 (2014).
- <sup>45</sup> T. Jeong and W. E. Pickett, *Phys. Rev. B* **70**, 075114 (2004).
- <sup>46</sup> B. Bradlyn, J. Cano, Z. Wang, M. Vergniory, C. Felser, R. Cava, and B. A. Bernevig, *Science* **353**, aaf5037 (2016).
- <sup>47</sup> P. Tang, Q. Zhou, and S.-C. Zhang, *Phys. Rev. Lett.* **119**, 206402 (2017).
- <sup>48</sup> T. Zhang, Z. Song, A. Alexandradinata, H. Weng, C. Fang, L. Lu, and Z. Fang, *Phys. Rev. Lett.* **120**, 016401 (2018).
- <sup>49</sup> A. Furusaki, *Science Bulletin* **62**, 788 (2017).
- <sup>50</sup> D. Pshenay-Severin, Y. V. Ivanov, A. Burkov, and A. Burkov, *J. Phys.: Condens. Matter* **30**, 135501 (2018).
- <sup>51</sup> G. Chang, S.-Y. Xu, B. J. Wieder, D. S. Sanchez, S.-M. Huang, I. Belopolski, T.-R. Chang, S. Zhang, A. Bansil, H. Lin, and M. Z. Hasan, *Phys. Rev. Lett.* **119**, 206401 (2017).
- <sup>52</sup> L. Ortenzi, I. I. Mazin, P. Blaha, and L. Boeri, *Phys. Rev. B* **86**, 064437 (2012).
- <sup>53</sup> R. Neddermann, R. Wartchow, and M. Binnewies, *Z. Anorg. Allg. Chem.* **624**, 733 (1998).
- <sup>54</sup> T. Sato, E. Ohta, and M. Sakata, *J. Phys. Soc. Jpn.* **52**, 3163 (1983).
- <sup>55</sup> T. Sato, E. Ohta, and M. Sakata, *J. Magn. Magn. Mater.* **61**, 205 (1986).
- <sup>56</sup> G. I. Kalishevich, *Russ. J. Phys. Chem. B* **43**, 1459 (1969).
- <sup>57</sup> V. P. Mineev and K. V. Samokhin, *Phys. Rev. B* **72**, 212504 (2005).
- <sup>58</sup> A. McCollam, B. Andraka, and S. R. Julian, *Phys. Rev. B* **88**, 075102 (2013).
- <sup>59</sup> See supplementary material at [LINK] for additional details concerning field-dependent frequencies and density-functional theory calculations.
- <sup>60</sup> D. Shoenberg, *Magnetic Oscillations in Metals* (Cambridge University Press, Cambridge, UK, 1984).
- <sup>61</sup> K. Koepnik and H. Eschrig, *Phys. Rev. B* **59**, 1743 (1999).
- <sup>62</sup> J. P. Perdew and Y. Wang, *Phys. Rev. B* **45**, 13244 (1992).
- <sup>63</sup> J. P. Perdew, K. Burke, and M. Ernzerhof, *Phys. Rev. Lett.* **77**, 3865 (1996).
- <sup>64</sup> M. Vergniory, L. Elcoro, C. Felser, B. Bernevig, and Z. Wang, arXiv:1807.10271 (2018).
- <sup>65</sup> J. H. P. v. Weeren and J. R. Anderson, *J. Phys. F: Met. Phys.* **3**, 2109 (1973).
- <sup>66</sup> A. Aguayo, I. I. Mazin, and D. J. Singh, *Phys. Rev. Lett.* **92**, 147201 (2004).
- <sup>67</sup> J. M. Ziman, *Models of disorder: the theoretical physics of homogeneously disordered systems* (Cambridge University Press, 1979).
- <sup>68</sup> D. Kasinathan, M. Wagner, K. Koepnik, R. Cardoso-Gil, Y. Grin, and H. Rosner, *Phys. Rev. B* **85**, 035207 (2012).
- <sup>69</sup> H. Takizawa, T. Sato, T. Endo, and M. Shimada, *J. Solid State Chem.* **73**, 40 (1988).
- <sup>70</sup> K. Lejaeghere, V. V. Speybroeck, G. V. Oost, and S. Cottenier, *Crit. Rev. Solid State* **39**, 1 (2014).
- <sup>71</sup> K. Lejaeghere, G. Bihlmayer, T. Björkman, P. Blaha, S. Blügel, V. Blum, D. Caliste, I. E. Castelli, S. J. Clark, A. D. Corso, *et al.*, *Science* **351**, aad3000 (2016).
- <sup>72</sup> H. Watanabe, N. Kazama, Y. Yamaguchi, and M. Ohashi, *J. Appl. Phys.* **40**, 1128 (1969).
- <sup>73</sup> B. Wang, Q. Lu, Y. Ge, K. Zhang, W. Xie, W.-M. Liu, and Y. Liu, *Phys. Rev. B* **96**, 134116 (2017).